Article:
Takeshita, S, Sadeghpour, A orcid.org/0000-0002-0475-7858, Sivaraman, D et al. (2 more authors) (2020) Solvents, CO2 and biopolymers: Structure formation in chitosan aerogel. Carbohydrate Polymers, 247. 116680. ISSN 0144-8617

https://doi.org/10.1016/j.carbpol.2020.116680

Solvents, CO_2 and Biopolymers: Structure Formation in Chitosan Aerogel

Satoru Takeshita[*,†,‡] *Amin Sadeghpour,*[§,^] *Deeptanshu Sivaraman,*[†] *Shanyu Zhao,*[†] *and Wim J. Malfait*[†]

[†]Laboratory for Building Energy Materials and Components, Empa, Swiss Federal Laboratories for Materials Science and Technology, Überlandstrasse 129, Dübendorf CH-8600, Switzerland

[‡]Research Institute for Chemical Process Technology, National Institute of Advanced Industrial Science and Technology (AIST), 1-1-1 Higashi, Tsukuba 3058565, Japan

[§]Center for X-ray Analytics, Empa, Swiss Federal Laboratories for Materials Science and Technology, Lerchenfeldstrasse 5, St. Gallen CH-9014, Switzerland

[^]Biomaterials Science Center, Department of Biomedical Engineering, University of Basel, Allschwil CH-4123, Switzerland

S.T. *s.takeshita@aist.go.jp; TEL: +81 29 861 2975; FAX +81 29 861 4567

A.S. amin.sadeghpour@unibas.ch

D.S. Deeptanshu.Sivaraman@empa.ch

S.Z. Shanyu.Zhao@empa.ch

W.M. wim.malfait@empa.ch

ABSTRACT

The functionality of biopolymer aerogels is inherently linked to its microstructure, which in turn depends on the synthesis protocol. Detailed investigations on the macroscopic size change and nanostructure formation during chitosan aerogel synthesis, reveal a new aspect of biopolymer aerogels that increases process flexibility. Formaldehyde-cross-linked chitosan gels retain a significant fraction of their original volume after solvent exchange into methanol (50.3%), ethanol (47.1%) or isopropanol (26.7%), but shrink dramatically during subsequent supercritical CO_2 processing (down to 4.9%, 3.5% and 3.7%, respectively). In contrast, chitosan gels shrink more strongly upon exchange into *n*-heptane (7.2%), a low affinity solvent, and retain this volume during CO_2 processing. Small-angle X-ray scattering confirms that the occurrence of the volumetric changes correlates with mesoporous network formation through physical coagulation in CO_2 or *n*-heptane. The structure formation step can be controlled by solvent–polymer and polymer–drying interactions, which would be a new tool to tailor the aerogel structure.

GRAPHICAL ABSTRACT

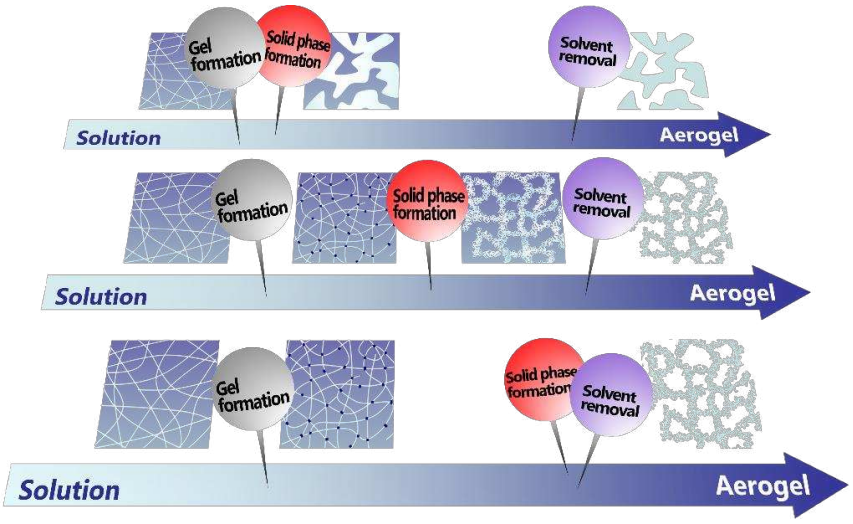

KEYWORDS

Aerogels, Biopolymers, Small-angle X-ray scattering, Supercritical drying

1. INTRODUCTION

Aerogels, highly porous solids with three-dimensional mesoporous structures, have become more and more attractive materials in both academia and industry in recent decades thanks to their large potential for energy-saving, energy-harvesting, biomedical, environmental remediation, and aerospace applications (Pierre & Pajonk, 2002; Aegerter et al., 2011; Randall et al., 2011; Smirnova & Gurikov, 2018). A lot of effort has been dedicated to microstructural control of aerogels because their favorable properties such as, high surface area, ultralow thermal conductivity (Jelle, 2011; Koebel et al., 2012), and unique mechanical, optical and acoustic properties (Tabata et al., 2012; Merli et al., 2018; Takeshita et al., 2019a), originate mainly from their three-dimensional pore structures. Aerogel production generally consists of three steps: wet gel making, washing/solvent exchange and drying. Classical studies on inorganic aerogels using scattering techniques had revealed that the initial gel making step is responsible for the formation of main porous skeletons (Craievich et al., 1986; Lours et al., 1990; Woignier et al., 1990; Pahl et al., 1991; Posselt et al., 1992; Hasmy et al., 1995; Rigacci et al., 2001; Reidy et al., 2001; Hu et al., 2001). Subsequent solvent exchange and drying steps make only minor modifications, such as internal primary particle formation in the skeletons (Perissinotto et al., 2015) and necking through Ostwald ripening in supercritical alcohol drying (Yoda & Ohshima, 1999). In particular, widely used supercritical CO_2 drying has been considered to preserve the microstructure because of inert nature of CO_2 and the absence of capillary forces during drying (Emmerling & Fricke, 1992).

Biopolymer aerogels rapidly became a hot topic in material science in late 2000s after the research trend shifted toward green and sustainable chemistry (Zhao et al., 2018; Takeshita et al., 2020; El-Naggar, 2020). Many researchers have focused on nano- and micro-fibrillated cellulose (Buesch et al., 2016; Plappert et al., 2017; De France et al., 2017) and chitin aerogels (Heath et al., 2013). In these cases, structure formation is simple: fibers with well-defined dimensions assemble to construct a three-dimensional aerogel structure at the gel formation step. Biopolymer aerogels starting from solution such as, chitosan (Takeshita et al., 2015, 2016, 2017a, b; Caro-León et al., 2018; Ganesan et al., 2018; El Kadib, 2020; Wei et al., 2020; Le Goff et al., 2020; Tabernero et al., 2020), pectin (White et al., 2010; Tkalec et al., 2015), and alginate (Valentin et al., 2005; Robitzer et al., 2008; Veronovski et al., 2012), show more complex structure formation, but in many cases, the initial gel formation step is still the structure-determining step. Typical examples include the physical coagulation of chitosan (Valentin et al., 2007; Baldino et al., 2014; Joan et al., 2018; López-Iglesias et al., 2020), pectin (Tkalec et al., 2015), and cellulose solution (Cai et al., 2008; Pircher et al., 2016) in antisolvents and/or by pH jump, in which gelation and solid phase formation, i.e. the phase separation between a dense solid skeleton and voids filled with solvent, occur simultaneously. Solvent exchange with antisolvent after the gelling is also responsible for structure formation through physical coagulation in some cases (Rudaz et al., 2014), but supercritical drying step was still considered to not affect the microstructure.

In the above-mentioned context, supercritical drying has been considered as the "gold standard" to make aerogels that preserve the microstructures from the wet gels, for both inorganic and organic systems. Very recently, our group found that the microstructure of chemically cross-linked chitosan gel can be drastically different before and after supercritical CO_2 processing (Takeshita et al., 2019b). In that study, cross-linking-induced gelation or solvent exchange into

methanol did not contribute much to the formation of the final rigid aerogel structure. Another interesting feature found in biopolymer aerogels is dynamic change in gel size during solvent exchange and even during supercritical drying (Gurikov et al., 2019), but the relation between macroscopic size and microstructure formation has not been investigated. Aside from its academic interest, excessive shrinkage of biopolymer aerogels during supercritical drying is also of practical importance because it reduces the volumetric yield of the process for a given autoclave volume and can thus present a significant barrier for industrial production.

Here, we use cross-linked chitosan aerogel as a model system to investigate the effect of different exchange solvents on shrinkage and structure formation in biopolymer aerogels. Specifically, the effect of solvent–polymer affinity on gel size is investigated, the aerogel nanostructure formation step is identified by small-angle X-ray scattering (SAXS), and shrinkage–structure formation correlation is established. The main purpose is to demonstrate gel-formation step control through solvent–polymer interactions as a general strategy for structure–property tailoring of biopolymer aerogels.

2. EXPERIMENTAL SECTION

2.1 Materials. Chitosan (Wako Pure Chemical Industry, deacetylation degree: 80%, viscosity: 20–200 mPa s at 5 g L^{-1} and 20 °C), acetic acid (VWR, 99.9%), formaldehyde aqueous solution (Sigma-Aldrich, 37 wt. %), methanol (Thommen Furler, 99%), ethanol (Alcosuisse, 99.9%), isopropanol (Thommen Furler, 99.5%), and *n*-heptane (Brenntag Schweizerhalle AG, UN 1206, 99%) were used without further purification. CO_2 (99.9%) was purchased from Messer Schweiz AG.

2.2 Aerogel synthesis. Chitosan was dissolved at 5 g L^{-1} in a 0.5 vol. % acetic acid solution to make a stock solution that was stored for at least 1 week. The stock solution (4.0 mL) was mixed with aqueous formaldehyde solution (1.0 mL, 37 wt. %) in a 30 mm (inner diameter) glass petri dish. The petri dish was placed in an airtight polypropylene container and kept at 60 °C for 24 h to complete gel formation and aging. The resulting hydrogel was soaked in organic solvents and its volumetric change was recorded as a function of time (detailed solvent exchange protocols in SI). After solvent exchange, the gel was placed in an autoclave (~50 mL in volume) with ~45 mL of the final exchange solvent and sealed in the supercritical drying system (Separax). The pressure of the system was gradually increased up to 160 bar over 1 h by introducing CO_2 without circulation, while the temperature was set at 80 °C. The solvent was extracted through CO_2 circulation at 160 bar for 4 h. Then, the pressure was gradually decreased to ambient pressure over 1 h, to yield an aerogel sample.

2.3 Volume, density and microstructure. The volumetric change of the hydrogels and organogels was determined from their diameter and height measured by caliper. The apparent density of the aerogel samples was calculated from its diameter, height and weight. Nitrogen sorption isotherms were acquired at 77 K with a gas-adsorption instrument (Micromeritics, 3flex) after 20 h of degassing at 50 °C and 0.06 mbar. The specific surface area was calculated from the isotherms from the low pressure range (P/P_0 between 0.07 and 0.30) using Brunauer–Emmett–Teller (BET) method. The pore properties were evaluated from the adsorption part of the isotherm using Barrett–Joyner–Halenda (BJH) analysis. The microstructure of the samples was observed with a field-emission scanning electron microscope (SEM, FEI, Nova NanoSEM 230) after application of a thin coating of conductive Pt.

2.4 SAXS measurements. Organogels for SAXS measurements were prepared directly in quartz capillaries (Hilgenberg, 1.5 mm width, 0.01 mm thick glass, 80 mm length). The 5 g L^{-1} chitosan solution described above was mixed with aqueous formaldehyde solution in a 4:1 volume ratio. This mixture was poured into the capillaries, sealed with paraffin film, and kept at 60 °C for 24 h to obtain hydrogels. The closed end of the capillary was broken in order to enable solvent exchange from both ends, and the capillaries were soaked in the designated solvents (methanol, water/ethanol → ethanol, water/isopropanol → isopropanol). The solvent was replaced at least 8 times over 7 days at room temperature to complete the solvent exchange, as monitored by diffusion of a dye (Fig. S2). As the heptane-exchanged wet gel could not be prepared directly in a capillary (due to drastic shrinkage), this sample was prepared by squeezing already solvent-exchanged wet gel into a capillary. The capillaries were sealed with wax prior loading into the vacuum environment of the sample chamber. The signals for sample and background were acquired 5 times, one hour for wet gels and 5 min for aerogels, and then averaged. Background measurements were conducted on capillaries filled with the relevant solvent. SAXS profiles were recorded with a Nanostar instrument (Bruker, Germany) equipped with a micro-focused X-ray source (Incoatec) with a beam spot size of about 400 μm, Cu Kα radiation (λ = 0.154 nm), and a VÅNTEC-2000 Xe-based gas avalanche detector placed 107 cm from the sample. The detector includes 2048 × 2048 pixels, each 68 × 68 μm^2 in size, and operates at a photon-counting rate of 0.5 per seconds. The minimum reliable scattering vector magnitude, q_{min}, is ~0.1 nm^{-1} with $q = (4\pi/\lambda)\sin\theta$ where 2θ is the scattering angle. All the experiments were carried out under vacuum (~0.01 mbar).

3. RESULTS AND DISCUSSION

3.1 Size change during the solvent exchange. Four organic solvents with a range in affinity for chitosan (methanol, ethanol, isopropanol, *n*-heptane) were selected based on physical and chemical restrictions of our processing equipment, and considering their future industrialization potential. A suitable solvent must be liquid at room temperature, miscible with water or ethanol to enable the stepwise exchange protocol, miscible with CO_2 under high pressure, compatible with the chemical resistivity of the seals in the supercritical dryer, and of limited toxicity. In addition to previously used methanol (Takeshita 2019b), ethanol and isopropanol were selected as longer alcohols with lower affinity for chitosan. *n*-heptane was included as an apolar solvent, because of its reduced toxicity, lower volatility compared to pentane and hexane, and miscibility with ethanol. Long-chain alkanes with limited miscibility with ethanol were not considered in the study. In addition to methanol, ethanol, isopropanol and *n*-heptane, we carried out preliminary tests with *n*-butanol and *n*-hexane (Fig. S6–S8 and Table S2), but these systems were not investigated fully because of incompatibilities with our supercritical drying equipment and process. The properties of typical solvents and the results of the preliminary investigations are summarized in Table S1 and Fig. S3–S5.

In a first step, we established solvent exchange protocols for methanol, ethanol, isopropanol, and *n*-heptane without complete collapse or drastic deformation of the gel. Table 1 and Figs. S3–S5 report on the solvent exchange screening results for both direct exchanges using pure solvents and stepwise exchanges using water/solvent mixtures. This investigation revealed that a systematic screening of different solvents via exactly the same protocol is difficult in the present study. Specifically, soaking the as-prepared hydrogel into pure water or water/methanol mixture expands and breaks the gel into slimy fractions, presumably because of the osmotic pressure caused by solute species (Takeshita et al., 2019b). The as-prepared hydrogels contain mostly water as the

pore fluid, but also some unreacted solute species from the cross-linking reaction. Direct immersion of the hydrogel into pure ethanol or isopropanol causes rapid shrinkage resulting in collapse or strong deformation. We, therefore, developed the following routes for further investigation of the methanol-, ethanol- and isopropanol-exchange: direct exchange with pure methanol, exchange into water/ethanol mixtures and then into pure ethanol, exchange into water/isopropanol mixtures and then into isopropanol. For *n*-heptane, the serial, stepwise exchange with water/ethanol, ethanol, ethanol/heptane and finally heptane successfully avoids fracturing of the gels. Note that solvent exchange is a dynamic process and the macroscopic size change is affected not only by the solvent composition, but also by the exchange history and exchange rate.

Table 1. Final size of wet gels, aerogels, and aerogel apparent densities prepared via different solvent exchange routes.

Solvent exchange route	$V_{Exchanged}/V_{Inital}$ (%)	$V_{Aerogel}/V_{Initial}$ (%)	Aerogel density (g cm^{-3})
Direct exchange with water	> 224 ± 12, broken	N/A	
Direct exchange with methanol*	50.3 ± 1.1	4.90 ± 0.05	0.083 ± 0.001
Direct exchange with ethanol	42.1 ± 3.8, deformed	4.47**	0.098**
Direct exchange with isopropanol	< 14.6 ± 0.8, broken	N/A	
Water/methanol → methanol	54.1 ± 3.6, broken	N/A	
Water/ethanol → ethanol	47.1 ± 1.2	3.45 ± 0.07	0.121 ± 0.002
Water/isopropanol → isopropanol	26.7 ± 0.3	3.65 ± 0.09	0.125 ± 0.003
Water/ethanol → ethanol → ethanol/heptane → heptane	7.2 ± 0.7	6.18 ± 0.19	0.067 ± 0.001
Methanol → methanol/ethanol → ethanol	45.1**	3.50**	0.118**
Methanol → methanol/isopropanol →isopropanol	35.7**	5.73**	0.073**
Blank (without adding solvent)	97.2 ± 1.4 (after 192 h)	N/A	

*Average of 6 samples and **1 sample, other routes are averages of 3 samples; $V_{Initial}$: volume of as-prepared hydrogel; $V_{Exchanged}$: gel volume after solvent exchange; $V_{Aerogel}$: volume of aerogel; N/A: not available.

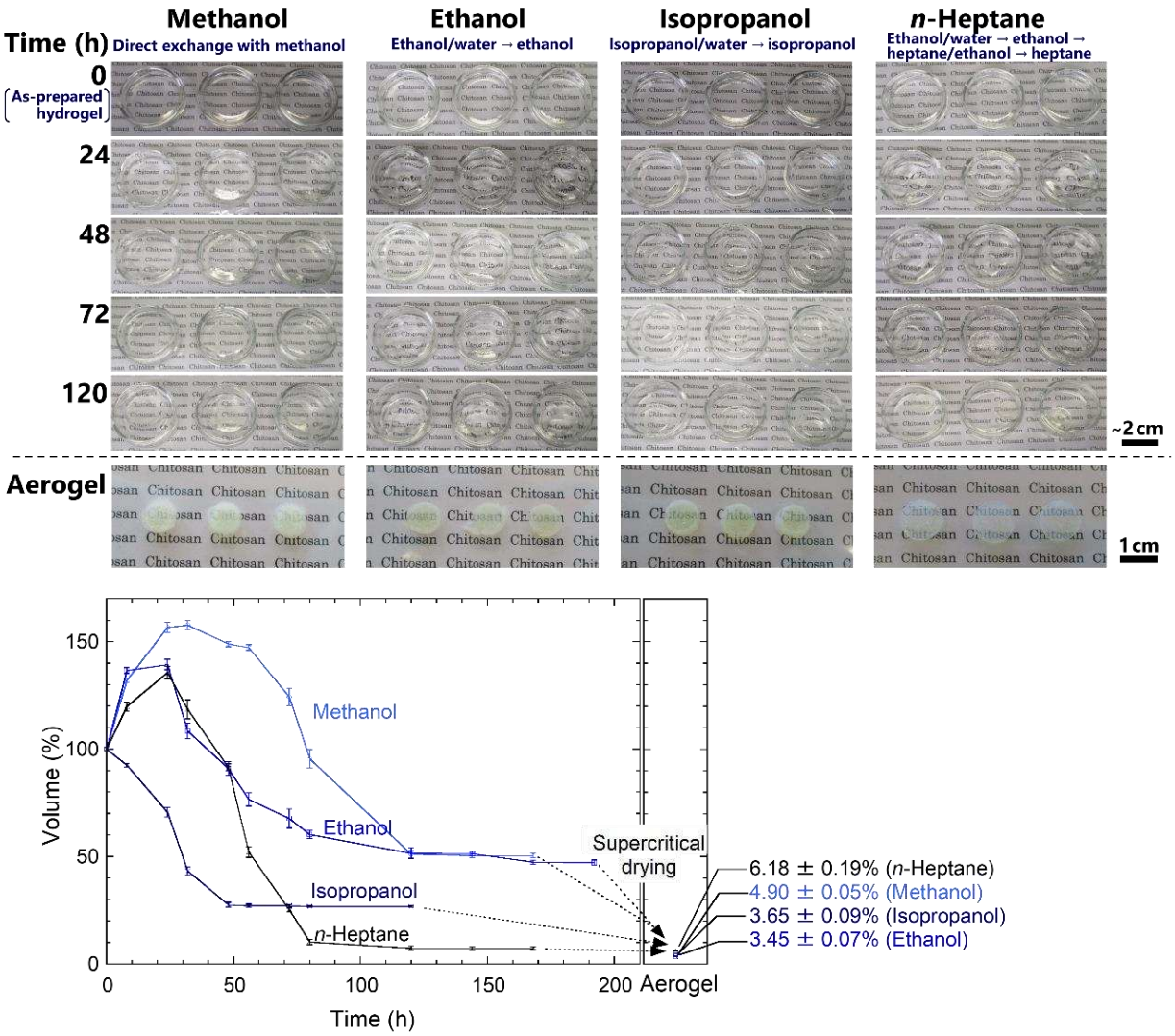

Fig. 1. Photographs of the gels as a function of solvent exchange time; three gels are shown for each treatment condition (top), and size change histories (bottom) of wet gels and aerogels prepared with different solvents.

Fig. 1 summarizes the size change history of wet gels with different solvent exchange protocols. Methanol- and ethanol-exchanged wet gels display an initial expansion up to ~140–150% and then subsequent shrinkage back to the ~50% of the initial volume. Isopropanol- and

heptane-exchanged samples converge to ~27% and ~7% of the initial gel volume, respectively. The initial increase upon immersion in methanol and water/ethanol is most likely related to the osmotic pressure. Previous studies have suggested that size changes of biopolymer gels are related to the difference in solubility parameters of polymers and solvents (Tripathi et al., 2018; Gurikov et al., 2019). In this study, we use the Flory–Huggins interaction parameter, χ, which is calculated from Hansen solubility parameters (Table S1, Hansen, 2007):

$$\chi = \frac{V\{(\delta_{d1}-\delta_{d2})^2+0.25(\delta_{p1}-\delta_{p2})^2+0.25(\delta_{h1}-\delta_{h2})^2\}}{RT} \quad (1)$$

where δ_{d1}, δ_{p1}, δ_{h1} and δ_{d2}, δ_{p2}, δ_{h2} are the Hansen solubility parameters for dispersion, polarity, and hydrogen bonds of the solvent and solute, respectively, R is the gas constant, T is temperature, and V is the molar volume of the solvent. The χ parameters between molecular chitosan and the solvents in our current work are water (0.85) < methanol (1.15) < ethanol (1.86) < isopropanol (3.24) < *n*-heptane (18.1), where a larger value means less affinity. These values roughly explain the tendency of the final sizes of solvent exchanged wet gels, methanol (~50%) > ethanol (~47%) > isopropanol (~27%) > *n*-heptane (~7%). We note that solubility parameters are useful for a qualitative estimation but have their limitations: i) chitosan is not in its neat state, but cross-linked and/or modified by the reaction with formaldehyde; and ii) solubility parameters cannot deal with ionic species, such as NH_3^+ of chitosan.

3.2 Aerogels size and microstructure. Fig. 1 and Table 1 summarize the final relative sizes and apparent densities of aerogels after supercritical CO_2 drying. All the aerogel samples have low to intermediate apparent densities (< 0.13 g cm^{-3}) and translucent, somewhat yellowish appearances, consistent with previous reports on methanol-exchanged aerogels (Takeshita & Yoda, 2015). The aerogels display a three-dimensional network of nanofiber-like structures (Fig. 2), but high-

resolution observation reveals that these fibrous components are comprised of particulate matter (see Fig. S9–S12 for different magnifications). Nitrogen adsorption measurements (Fig. 3 and Table S3) show that the aerogels have type IV mesoporous structures with between 500 and 600 $m^2\ g^{-1}$ of surface area and between 2 and 4 $cm^3\ g^{-1}$ of BJH pore volume. The BJH pore volume correlates negatively with apparent density. In particular, heptane-exchanged aerogels exhibit the lowest density (~0.067 g cm^{-3}) and the highest pore volume and surface area.

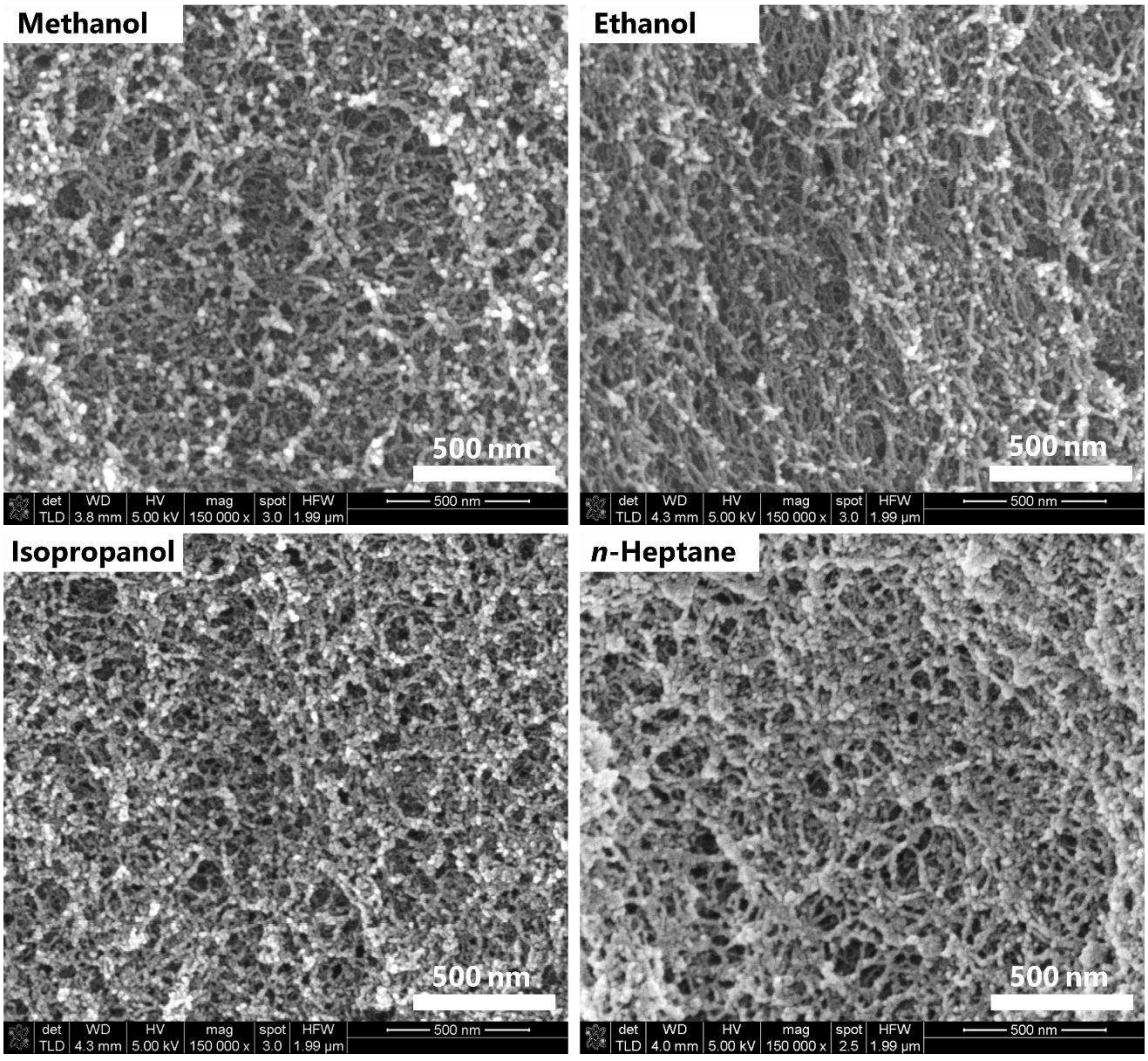

Fig. 2. SEM images of aerogels prepared with different solvent exchange protocols.

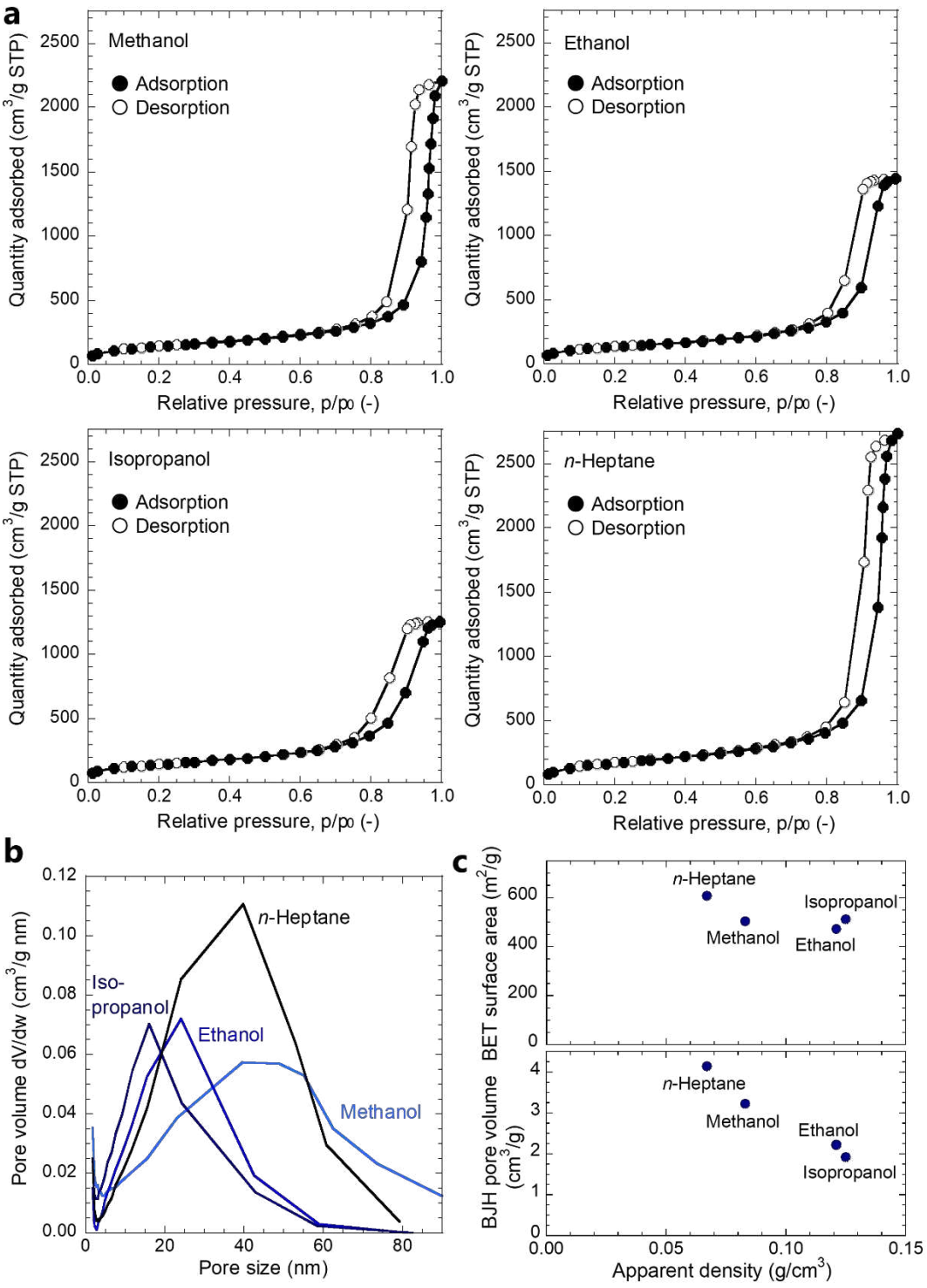

220

221 **Fig. 3.** N_2 adsorption profiles of aerogels prepared with different solvent exchange protocols: a)
222 isotherms, b) pore size distributions, and c) variations in surface area and pore volume with aerogel
223 density.

The size change before and after supercritical drying (Fig. 1) leads to the following observations. For methanol-, ethanol- and isopropanol-exchanged samples, the final aerogel size is 3–5% of the initial volume, regardless of the solvent, and the most of the shrinkage occurs during supercritical drying. Exchange into heptane leads to less overall shrinkage, 6% of the initial volume is retained, and the volume change occurs almost entirely during the solvent exchange, with only minor shrinkage during subsequent supercritical drying.

3.3 Relation between size and structure formation. Fig. 4 represents the SAXS profiles and the Kratky plots of wet gels and aerogels as a function of the pore solvents. The SAXS data of the methanol-, ethanol- and isopropanol-exchanged wet gels (Fig. 4a) display a slope close to −2, which is indicative of mainly Gaussian chain configurations. These plots resemble that of the as-prepared hydrogel, which displays a Gaussian-chain-like profile from single polysaccharide chains without evidence for solid structure formation (Takeshita et al., 2019b). The Kratky plots of these samples represent plateaus, also consistent with Gaussian chain-like scattering behavior. They can be fitted with the original Ornstein-Zernike equation (detailed fits are in SI). The correlation length increases from 4.2 ± 0.1 to 6.2 ± 0.4 nm with increasing χ value, i.e. in the order of methanol, ethanol, and isopropanol. On the other hand, the heptane-exchanged wet gel (the top plot in Fig. 4a) displays two scattering regimes with slopes of −1.25 at low q (< ~0.5 nm^{-1}) and −3.53 at high q (> ~0.6 nm^{-1}), and share a striking resemblance to the aerogel profiles (Fig. 4b). In addition, the scattering profile resembles that of nanofibrillated cellulose wet gels (Leppänen et al., 2010). In the Kratky plot, a broad bell-shaped peak indicates collapsed chitosan chains. Qualitatively, the heptane-exchanged gel has a much stronger scattering intensity of X-ray, indicative of the presence of larger scattering objects. The SAXS curves of the aerogel samples are all quite similar, with two

different slopes, −1.4 to −1.6 at low q (< ~0.5 nm^{-1}) and ~ −4 at high q (> ~0.6 nm^{-1}). These types of SAXS curves are strongly reminiscent to those of mesoporous silica and cellulose aerogels (Santos et al., 1987; Plappert et al., 2018). The SAXS data verify that, in contrast to the alcohol-exchanged wet gels, an aerogel-like nanostructure has been formed during the heptane-exchange wet gel processing step, i.e. prior to supercritical CO_2 drying. (Fig. 4c). The stage at which the structure forms for different gels is also reflected in their corresponding volumes: moderate shrinkage during solvent exchange and high shrinkage during CO_2 processing for the alcohol exchanged gels versus high shrinkage during heptane exchange followed by minimal shrinkage during CO_2 processing.

In our previous in situ observations of supercritical drying, we demonstrated that large shrinkage occurs at the initial stage of supercritical drying, i.e. when CO_2 is introduced to the autoclave (Takeshita et al., 2019b). We interpreted this observation by considering supercritical/liquid CO_2 as a "solvent". The solubility parameters of CO_2 are a function of temperature and pressure (see Table S1 for details), and the χ parameter of CO_2 at 80 °C and 160 bar is 15.7 (Hansen, 2007). This value is in line with that of *n*-heptane during solvent exchange (χ = 18.1), but much larger than for methanol (χ = 1.15), ethanol (χ = 1.86) or isopropanol (χ = 3.24). Thus, heptane and CO_2 have a similar (low) affinity to chitosan. The similarity in solvent–biopolymer interactions results in the very limited shrinkage during supercritical CO_2 drying of heptane-exchanged gels. We note that the actual solvent composition and its state inside the gel during drying are more complicated because CO_2 would be closer to liquid state at the beginning of the CO_2 introduction step (e.g. liquid CO_2 at 25 °C and 60 bar has a larger χ of 60.5).

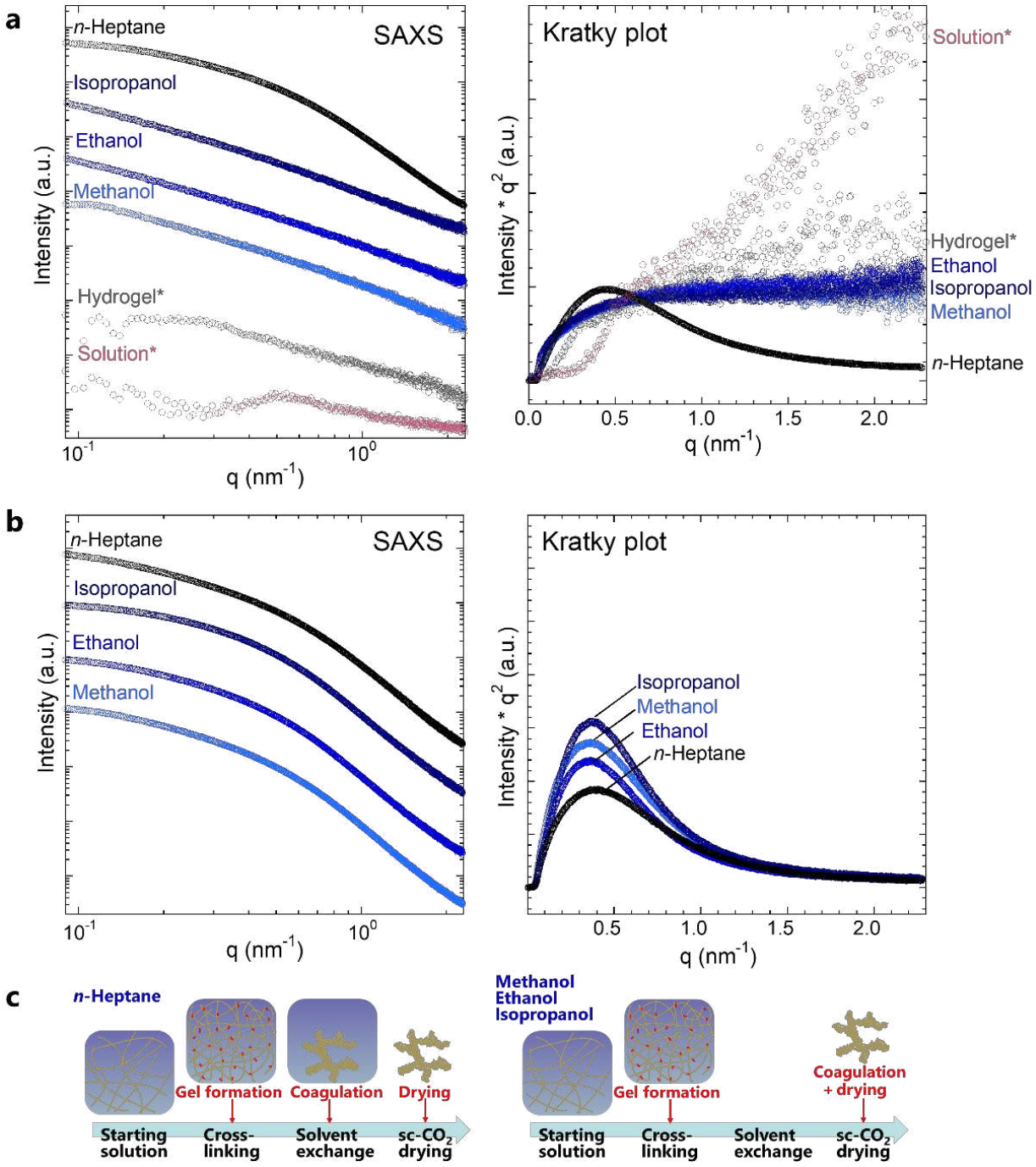

Fig. 4. SAXS profiles and their Kratky plots of a) wet gels (Kratky plots are normalized at the shoulder), and b) aerogels prepared with different solvent exchange protocols. The data for the chitosan solution and as-prepared hydrogel data are replotted from our previous study (Takeshita et al., 2019b). c) Schematic representation of structure formation processes of aerogels.

Based on the SAXS data and size change histories, we conclude that large volumetric changes are accompanied with aerogel-like nanostructure formation through the interaction of the chitosan chains with antisolvent leading to physical coagulation. Methanol, ethanol and isopropanol are also known antisolvents for neat chitosan chains, so one would intuitively expect physical coagulation and hence structure formation also in these solvents, but this idea can be discarded by the SAXS data (Fig. 4a) that directly elucidate the molecular level interactions and nanoscale structures formation. We suggest that the 3D network of formaldehyde-cross-linked chitosan, and/or the chemical modification of chitosan with formaldehyde kinetically inhibits coagulation.

3.4 Solvent control on shrinkage and structure formation for tailored structures and processes. The present results demonstrate that the gel/aerogel structure can be formed at any step from gel making, solvent exchange to supercritical drying. To generalize this idea, we can describe aerogel production protocols based on three key events: i) gel formation, ii) solid phase formation and iii) solvent removal (Fig. 5). For example, silica aerogel preparation via a colloidal route typically follows the order of ii) → i) → iii) (Fig. 5a), while the present cases are described as i) → ii + iii) for the alcohol-exchanged gels and i) → ii) → iii) for the heptane-exchange protocol. In contrast to alcohol-exchanged systems, the solid phase formation and the solvent removal steps are clearly separated for the heptane-exchanged system (Fig. 5c and 5d). Moreover, the control on the structural formation/shrinkage leads to a more efficient use of autoclave volume. We have shown that heptane-exchange induced shrinkage (and structure formation) prior to drying eliminates CO_2 induced shrinkage almost entirely, thereby increasing the volumetric yield of the supercritical drying equipment by a factor of ~7. Another potential benefit would be a toolbox for designing the fabrication process of biopolymer aerogels for more precise structural control.

Typical aerogels prepared via physical coagulation of chitosan (Valentin et al., 2007), pectin (Tkalec et al., 2015) and cellulose from solution (Pircher et al., 2016) have micrometer-sized structural features and opaque appearances (multiple light scattering). In contrast, formaldehyde-cross-linked chitosan aerogel, used in this study, has a highly homogeneous microstructure and only inhomogeneity in nanoscale. Such nanoscale properties lead to a system with high transparency, and the highest surface area and the lowest thermal conductivity among the biopolymer aerogels reported to date (Takeshita & Yoda, 2018). During synthesis, the concurrent appearance of i) gelation and ii) the solid phase formations occurs in the former systems (Fig. 5b), but are clearly separated in the latter one. We suggest that this is important to avoid micrometer-sized phase separation and increases the control on the formation of highly mesoporous transparent aerogels.

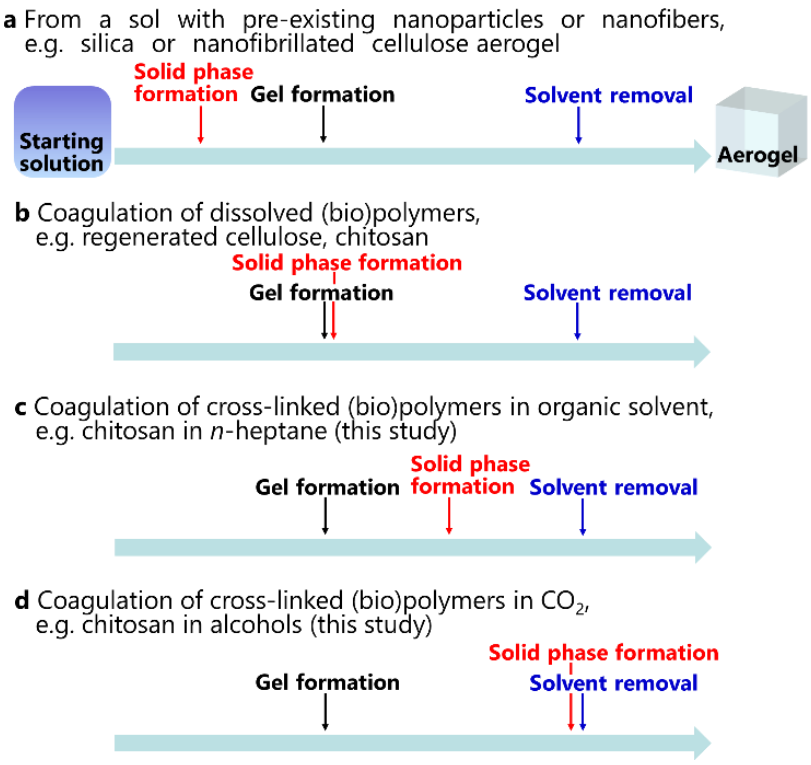

Fig. 5. Microstructure formation stages of aerogels with different orders of gel formation, solid phase formation, and solvent removal.

4. CONCLUSIONS

SAXS investigations revealed that the structure formation step in cross-linked chitosan aerogels is controlled by the polymer–solvent affinity. For solvents with a relatively good affinity, such as alcohols, the aerogel structure is not formed at the solvent exchange step, but during subsequent drying step and interactions with CO_2. For a low affinity solvent such as *n*-heptane, the solvent exchange itself induces the formation of an aerogel-like structure and a concomitant drastic shrinkage of the gel. In this respect, the solvent parameters can be used to estimate the interactions with biopolymer and predict the structure formation in aerogels. Finally, the generalization of the aerogel production process proposed in this study helps to establish a strategy to precisely control aerogel structure and to develop processing approaches with high degree of robustness. We propose that other biopolymer and synthetic polymer systems that display drastic size changes during solvent exchange or supercritical drying must be revisited from the viewpoint of structure formation at the nanoscale. This would serve as a key approach to answer long-standing questions for aerogel researchers, e.g. why transparent biopolymer aerogels are rare.

ACKNOWLEDGMENTS

This work was partially supported by JSPS KAKENHI Grant Number JP19K05193 and SNF grant 200021_179000 from the Swiss National Science Foundation.

Note

The cross-linked chitosan aerogel is the subject of a Japanese patent application by AIST.

Appendix A. Supplementary data

Additional experimental details and size change records, solubility parameters, SEM images, SAXS fitting details can be found online at https://doi.org/XXXXXXXXX.

REFERENCES

Aegerter, M. A., Leventis, N., & Koebel, M. M. Eds. (2011). *Aerogels Handbook*, Springer.

Baldino, L., Cardea, S., De Marco, I., & Reverchon, E. (2014). Chitosan scaffolds formation by a supercritical freeze extraction process. *J. Supercrit. Fluids*, *90*, 27–34.

Buesch, C., Smith, S. W., Eschbach, P., Conley, J. F., & Simonsen, J. (2016). The Microstructure of Cellulose Nanocrystal Aerogels as Revealed by Transmission Electron Microscope Tomography. *Biomacromolecules*, *17*, 2956–2962.

Cai, J., Kimura, S., Wada, M., Kuga, S., & Zhang, L. (2008). Cellulose Aerogels from Aqueous Alkali Hydroxide–Urea Solution. *ChemSusChem*, *1*, 149–151.

Caro-León, F. J., Argüelles-Monal, W., Carvajal-Millán, E., López-Franco, Y. L., Goycoolea-Valencia, F. M., & Román del Barrio, J. S. (2018). Production and characterization of supercritical CO_2 dried chitosan nanoparticles as novel carrier device. *Carbohydr. Polym.*, *198*, 556–562.

Craievich, A., Aegerter, M. A., dos Santos, D. I., Woignier, T., & Zarzycki, J. (1986). A SAXS study of silica aerogels. *J. Non-Cryst. Solids*, *86*, 394–406.

De France, K. J., Hoare, T., & Cranston, E. D. (2017). Review of Hydrogels and Aerogels Containing Nanocellulose. *Chem. Mater.*, *29*, 4609–4631.

El Kadib, A. (2020). Green and Functional Aerogels by Macromolecular and Textural Engineering of Chitosan Microspheres. *Chem. Record*, in press. doi.org/10.1002/tcr.201900089.

El-Naggar, M. E. (2020). Synthesis, drying process and medical application of polysaccharide-based aerogels. *Int. J. Biol. Macromol.*, *145*, 1115–1128.

Emmerling, A., & Fricke, J. (1992). Small angle scattering and the structure of aerogels. *J. Non-Cryst. Solids*, *145*, 113–120.

Ganesan, K., Heyer, M., Ratke, L., & Milow, B. (2018). Facile Preparation of Nanofibrillar Networks of "Ureido–Chitin" Containing Ureido and Amine as Chelating Functional Groups. *Chem. Eur. J.*, *24*, 19332–19340.

Gurikov, P., Raman, S. P., Griffin, J. S., Steiner III, S. A., & Smirnova, I. (2019). 110th Anniversary: Solvent Exchange in the Processing of Biopolymer Aerogels: Current Status and Open Questions. *Ind. Eng. Chem. Res.*, *58*, 18590–18600.

Hansen, C. M. Ed. (2007). *Hansen Solubility Parameters: A User's Handbook* (2nd ed.), CRC Press, Boca Raton.

Hasmy, A., Foret, M., Anglaret, E., Pelous, J., Vacher, R., & Jullien, R. (1995). Small-angle neutron scattering of aerogels: simulations and experiments. *J. Non-Cryst. Solids*, *186*, 118–130.

Heath, L., Zhu, L., & Thielemans, W. (2013). Chitin Nanowhisker Aerogels. *ChemSusChem*, *6*, 537–544.

Hu, X., Littrel, K., Ji, S., Pickles, D. G., & Risen, Jr., W. M. (2001). Characterization of silica-polymer aerogel composites by small-angle neutron scattering and transmission electron microscopy. *J. Non-Cryst. Solids*, *288*, 184–190.

Jelle, B. P. (2011). Traditional, state-of-the-art and future thermal building insulation materials and solutions - Properties, requirements and possibilities. *Energy Build.*, *43*, 2549–2563.

Joan, C. L.-I., Ardao, B. I., Monteiro, F. J., Alvarez-Lorenzo, C., Gómez-Amoza, J. L., & García-González, C. A. (2018). Vancomycin-loaded chitosan aerogel particles for chronic wound applications. *Carbohydr. Polym.*, *204*, 223–231.

Koebel, M., Rigacci, A., & Achard, P. (2012). Aerogel-based thermal superinsulation: an overview. *J. Sol-Gel Sci. Technol.*, *63*, 315–339.

Le Goff, R., Mahé, O., Le Coz-Botrel, R., Malo, S., Goupil, J.-M., Brière, J.-F., & Dez, I. (2020). Insight in chitosan aerogels derivatives -Application in catalysis. *React. Funct. Polym.*, *146*, 104393-1–9.

Leppänen, K., Pirkkalainen, K., Penttilä, P., Sievänen, J., Kotelnikova, N., & Serimaa, R. (2010). Small-angle x-ray scattering study on the structure of microcrystalline and nanofibrillated cellulose. *J. Phys.: Conf. Ser.*, *247*, 012030-1–4.

López-Iglesias, C., Barros, J., Ardao, I., Gurikov, P., Monteiro, F. J., Smirnova, I., Alvarez-Lorenzo, C., & García-González, C. A. (2020). Jet Cutting Technique for the Production of Chitosan Aerogel Microparticles Loaded with Vancomycin. *Polymers*, *12*, 273-1–13.

389 Lours, T., Zarzycki, J., Craievich, A. F., & Aegerter, M. A. (1990). Textural characteristics of
390 silica aerogels from SAXS experiments. *J. Non-Cryst. Solids*, *121*, 216–220.

391 Merli, F., Anderson, A. M., Carroll, M. K., & Buratti, C. (2018). Acoustic measurements on
392 monolithic aerogel samples and application of the selected solutions to standard window systems.
393 *Appl. Acoust.*, *142*, 123–131.

394 Pahl, R., Bonse, U., Pekala, R. W., & Kinney, J. H. (1991). SAXS investigations on organic
395 aerogels. *J. Appl. Crystallogr.*, *24*, 771–776.

396 Perissinotto, A. P., Awano, C. M., Donatti, D. A., de Vicente, F. S., & Vollet, D. R. (2015). Mass
397 and Surface Fractal in Supercritical Dried Silica Aerogels Prepared with Additions of Sodium
398 Dodecyl Sulfate. *Langmuir*, *31*, 562–568.

399 Pierre, A. C., & Pajonk, G. M. (2002). Chemistry of Aerogels and Their Applications, *Chem. Rev.*,
400 *102*, 4243–4266.

401 Pircher, N., Carbajal, L., Schimper, C., Bacher, M., Rennhofer, H., Nedelec, J.-M., Lichtenegger,
402 H. C., Rosenau, T., & Liebner, F. (2016). Impact of selected solvent systems on the pore and solid
403 structure of cellulose aerogels. *Cellulose*, *23*, 1949–1966.

404 Plappert, S. F., Nedelec, J.-M., Rennhofer, H., Lichtenegger, H. C., & Liebner, F. W. (2017). Strain
405 Hardening and Pore Size Harmonization by Uniaxial Densification: A Facile Approach toward
406 Superinsulating Aerogels from Nematic Nanofibrillated 2,3-Dicarboxyl Cellulose. *Chem. Mater.*,
407 *29*, 6630–6641.

Plappert, S. F., Nedelec, J.-M., Rennhofer, H., Lichtenegger, H. C., Bernstorff, S., & Liebner, F. W. (2018). Self-Assembly of Cellulose in Super-Cooled Ionic Liquid under the Impact of Decelerated Antisolvent Infusion: An Approach toward Anisotropic Gels and Aerogels. *Biomacromolecules*, *19*, 4411–4422.

Posselt, D., Pedersen, J. S., & Mortensen, K. (1992). A SANS investigation on absolute scale of a homologous series of base-catalysed silica aerogels. *J. Non-Cryst. Solids*, *145*, 128–132.

Randall, J. P., Meador, M. A. B., & Jana, S. C. (2011). Tailoring Mechanical Properties of Aerogels for Aerospace Applications. *ACS Appl. Mater. Interfaces*, *3*, 613–626.

Reidy, R. F., Allen, A. J., & Krueger, S. (2001). Small angle neutron scattering characterization of colloidal and fractal aerogels. *J. Non-Cryst. Solids*, *285*, 181–186.

Rigacci, A., Ehrburger-Dolle, F., Geissler, E., Chevalier, B., Sallée, H., Achard, P., Barbieri, O., Berthon, S., Bley, F., Livet, F., Pajonk, G. M., Pinto, N., & Rochas, C. (2001). Investigation of the multi-scale structure of silica aerogels by SAXS. *J. Non-Cryst. Solids*, *285*, 187–193.

Robitzer, M., David, L., Rochas, C., Di Renzo, F., & Quignard, F. (2008). Nanostructure of Calcium Alginate Aerogels Obtained from Multistep Solvent Exchange Route. *Langmuir*, *24*, 12547–12552.

Rudaz, C., Courson, R., Bonnet, L., Calas-Etienne, S., Sallée, H., & Budtova, T. (2014). Aeropectin: Fully Biomass-Based Mechanically Strong and Thermal Superinsulating Aerogel. *Biomacromolecules*, *15*, 2188–2195.

Santos, D. I., Aegerter, M. A., Craievich, A. F., Lours, T., & Zarzycki, J. (1987). Structural studies of fractal silica aerogels. *J. Non-Cryst. Solids*, *95–96*, 1143–1150.

Smirnova, I., & Gurikov, P. (2018). Aerogel production: Current status, research directions, and future opportunities. *J. Supercrit. Fluids*, *134*, 228–233.

Tabata, M., Adachi, I., Kawai, H., Kubo, M., & Sato T. (2012). Recent Progress in Silica Aerogel Cherenkov Radiator. *Phys. Proc.*, *37*, 642–649.

Tabernero, A., Baldino, L., Misol, A., Cardea, S., & Martín del Valle, E. M. (2020). Role of rheological properties on physical chitosan aerogels obtained by supercritical drying. *Carbohydr. Polym.*, *233*, 115850-1–8.

Takeshita, S., & Yoda, S. (2015). Chitosan Aerogels: Transparent, Flexible Thermal Insulators. *Chem. Mater.*, *27*, 7569–7572.

Takeshita, S., Takebayashi, Y., Nakamura, H., & Yoda, S. (2016). Gas-Responsive Photoluminescence of YVO_4:Eu^{3+} Nanoparticles Dispersed in an Ultralight, Three-Dimensional Nanofiber Network. *Chem. Mater.*, *28*, 8466–8469.

Takeshita, S., Konishi, A., Takebayashi, Y., Yoda, S., & Otake, K. (2017a). Aldehyde Approach to Hydrophobic Modification of Chitosan Aerogels. *Biomacromolecules*, *18*, 2172–2178.

Takeshita, S., & Yoda, S. (2017b). Translucent, hydrophobic, and mechanically tough aerogels constructed from trimethylsilylated chitosan nanofibers. *Nanoscale*, *9*, 12311–12315.

Takeshita, S., & Yoda, S. (2018). Upscaled Preparation of Trimethylsilylated Chitosan Aerogel. *Ind. Eng. Chem. Res.*, *57*, 10421–10430.

Takeshita, S., Akasaka, S., & Yoda, S. (2019a). Structural and acoustic properties of transparent chitosan aerogel. *Mater. Lett.*, *254*, 258–261.

Takeshita, S., Sadeghpour, A., Malfait, W. J., Konishi, A., Otake, K., & Yoda, S. (2019b). Formation of Nanofibrous Structure in Biopolymer Aerogel during Supercritical CO_2 Processing: The Case of Chitosan Aerogel. *Biomacromolecules*, *20*, 2051–2057.

Takeshita, S., Zhao, S., Malfait, W. J., & Koebel, M. M. (2020). Chemistry of Chitosan Aerogels: Three–Dimensional Pore Control for Tailored Applications. *Angew. Chem. Int. Ed.*, in press. doi.org/10.1002/anie.202003053

Tkalec, G., Knez, Ž., & Novak, Z. (2015). Fast production of high-methoxyl pectin aerogels for enhancing the bioavailability of low-soluble drugs. *J. Supercrit. Fluids*, *106*, 16–22.

Tripathi, A., Parsons, G. N., Khan, S. A., & Rojas, O. J. (2018). Synthesis of organic aerogels with tailorable morphology and strength by controlled solvent swelling Hansen solubility. *Sci. Rep.*, *8*, 2106-1–12.

Valentin, R., Molvinger, K., Quignard, F., & Di Renzo, F. (2005). Methods to Analyse the Texture of Alginate Aerogel Microspheres. *Macromol. Symp.*, *222*, 93–102.

Valentin, R., Bonelli, B., Garrone, E., Di Renzo, F., & Quignard, F. (2007). Accessibility of the Functional Groups of Chitosan Aerogel Probed by FT-IR-Monitored Deuteration. *Biomacromolecules*, *8*, 3646–3650.

Veronovski, A., Novak, Z., & Knez, Ž. (2012). Synthesis and Use of Organic Biodegradable Aerogels as Drug Carriers. *J. Biomater. Sci. Polym. Ed.*, *23*, 873–886.

Wei, S., Ching, Y. C., & Chuah, C. H. (2020). Synthesis of chitosan aerogels as promising carriers for drug delivery: A review. *Carbohydr. Polym.*, *231*, 115744-1–14.

White, R. J., Budarin, V. L., & Clark, J. H. (2010). Pectin-Derived Porous Materials. *Chem. Eur. J.*, *16*, 1326–1335.

Woignier, T., Phalippou, J., Vacher, R., Pelous, J., & Courtens, E. (1990). Different kinds of fractal structures in silica aerogels. *J. Non-Cryst. Solids*, *121*, 198–201.

Yoda, S., & Ohshima, S. (1999). Supercritical drying media modification for silica aerogel preparation. *J. Non-Cryst. Solids*, *248*, 224–234.

Zhao, S., Malfait, W. J., Alburquerque, N. G., Koebel, M. M., & Nyström, G. (2018). Biopolymer Aerogels and Foams: Chemistry, Properties, and Applications. *Angew. Chem. Int. Ed.*, *57*, 7580–7608.